Boundary-Layer Meteorology
https://doi.org/10.1007/s10546-021-00627-z

RESEARCH ARTICLE

Small-Scale Spatial Variation of the Nocturnal Wind Field

L. Mahrt[1] · **D. Belušić**[2] · **O. Acevedo**[3]

Received: 12 January 2021 / Accepted: 22 April 2021

Abstract
This study examines the spatial variability of the nocturnal wind field using eight networks of surface observations ranging in horizontal width from 500 m to 65 km. The wind field is partitioned into small-scale variability (submeso motions) and the spatially-averaged wind vector. The vector-averaged wind is analogous to the wind resolved by a numerical model, posed here in terms of the wind that is vector averaged over an observational network. The small-scale variability represents the unresolved subgrid (sub-network) variation estimated in terms of the spatial variation of the wind vector within the observational domain. The bulk formula for the spatially-averaged heat flux is modified to account for the subgrid variation of the wind field. Investigation of the spatial variability of the wind field is also motivated by the need to estimate the representativeness of observations of the wind vector at an individual measurement site with respect to the wind field over the surrounding landscape. The small-scale variability of the observed wind field is contrasted between the networks as a function of the spatially-averaged wind vector, stratification, size of the network, and the topography. A strong dependence on topography emerges in spite of different instrumentation, deployment strategy, and processing for each network. Even weak topography can be important. A better design for future observational networks is briefly discussed.

Keywords Local spatial variation · Nocturnal boundary layer · Stratified turbulence · Submeso · Topography

1 Introduction

Local spatial variations of the surface wind field directly affect dispersion in the statically stable nocturnal boundary layer and indirectly influence the surface temperature and other meteorological variables. Horizontal variation of the surface wind can be induced by topography, surface heterogeneity, spatial variations of turbulence forced by downward mixing, and numerous transient motions. The horizontal variation of the surface wind may not be

✉ L. Mahrt
mahrt@nwra.com

[1] NorthWest Research Associates, 2171 NW Kari Pl, Corvallis, OR 97330, USA

[2] Swedish Meteorological and Hydrological Institute (SMHI), 601 76 Norrköping, Sweden

[3] Universidade Federal de Santa Maria, Santa Maria, RS 97105-900, Brazil

Published online: 27 May 2021

resolved by numerical models nor spatially resolved by standard observations. The different influences upon the surface wind may interact. For example, topography can generate propagating transient modes that modify local katabatic flows, while katabatic flows can themselves initiate local oscillations (Fedorovich and Shapiro 2009). Cuxart et al. (2007) examined the convergence of katabatic flows into a valley cold pool, which then descended down the valley and then subsequently over the sea as a land breeze. This regime corresponds to substantial horizontal variation of the wind vector. Mortarini et al. (2018) detailed the potential complexity of nocturnal boundary layers in terms of the interaction between the turbulence, multiple circulations driven by surface heterogeneity, and low-level jets.

Abraham and Monahan (2020) found that the spatial variability of the wind field generates spatial transitions between weakly stable and very stable regimes. They found that weakly stable regimes are coherent over larger spatial scales compared to very stable regimes where mixing is weak and generally fine scale. Grachev et al. (2013) provide a detailed illustration of the very stable case. Downward bursting associated with shear instability that develops from a perturbed cold pool can lead to significant horizontal variations of the surface wind (Zhou and Chow 2014). Turbulence bursting downward associated with low-level jets can induce significant variability of the flow near the surface (Cava et al. 2019b). The horizontal variation of the low-level jet and boundary-layer turbulence can be two-way coupled (Banta et al. 2003) and impose length scales on the underlying boundary layer (Grisogono et al. 2007; Grisogono and Rajak 2009), or the low-level jet and the underlying boundary layer can be decoupled (Grisogono and Axelsen 2012). Low-level jets are often generated by baroclinity over sloped terrain and Coriolis effects. Coriolis effects are associated with an inertial oscillation that is triggered by rapid decay of the turbulence during the evening boundary-layer transition. The spatial variation of inertial oscillations is generally resolved by numerical models. The effects of baroclinity and the inertial oscillation on low-level jets are unified in the relatively simple approach of Shapiro et al. (2016). Low-level jets confined to basins (Cuxart 2008; Cuxart et al. 2012) can lead to spatial variations of the surface wind that are not resolved by large-scale numerical models.

Finnigan et al. (2020) partitioned topographical influences on the spatial variation of the wind field into katabatic flows and mechanical modification of the airflow over hills. They extensively surveyed both subjects including the impact of vegetation. Finnigan et al. (2020) summarized how the wind field can vary in the downwind direction due to acceleration at the hill crest and downwind recirculation (separation bubble), and lee or wake turbulence. They also surveyed observational strategies and reviewed modelling approaches ranging from idealized flows based on scaling arguments to flows based on eddy-resolving numerical models. The potential complexity of flows in complex terrain within the Perdigão network, examined in our study, is illustrated in Fig. 3 of Fernando et al. (2017). Lehner and Rotach (2018) systematically surveyed studies of flows over steeper mountainous terrain. Rotach et al. (2017) discuss the observational and analysis strategies for steeper terrain. More isolated hills and mountains can lead to flow separation due to low-level flow around the topographical feature and over the topographical feature at higher levels (Leo et al. 2016). Topographically-induced circulations sometimes transport quantities vertically that become important compared to the vertical transport by the turbulence (Rotach and Zardi 2007).

Local katabatic flows or their spatial variability down the slope are often unresolved in numerical models and unresolved by the usual observational networks. A wind maximum develops, commonly below 10 m, and its spatial variability leads to spatial variability of the surface wind. Oldroyd et al. (2014) examined katabatic flows on steeper slopes where a low-level wind maximum was particularly well defined during the evening transition (Nadeau et al. 2013). Acceleration of katabatic flow down the slope sometimes corresponds to significant

spatial variation of the surface wind speed (Grachev et al. 2016). The analysis of observed fluxes over sloped terrain is more complicated than over a flat surface. With steeper slopes, the analysis of the data and the interpretation of buoyancy becomes more complex, which requires modification of the coordinate system (Oldroyd et al. 2016a) and reinterpretation of buoyancy fluxes (Oldroyd et al. 2016b). Even over weaker slopes, such as typical down-valley slopes, Stiperski and Rotach (2016) find that the choice of analysis procedures, including coordinate rotation, can be important. Pfister et al. (2017) showed that the surface drainage flow might be dominated by larger-scale slopes rather than the local slope. Because of the complexity of observed katabatic flows, simple models offer insight into some aspects of drainage flows (Cuxart et al. 2020). Fedorovich and Shapiro (2009, 2017) have modified simple models to provide improved solutions that predict oscillations generated by katabatic flows. The frequency is approximately $N \sin(\alpha)$ where α is the slope and N is the Brunt–Väisälä frequency. Fedorovich and Shapiro (2017) examine this problem in detail including interpretation of the important citations. This locally generated oscillation may occur in addition to submeso modes (Vercauteren et al. 2019) that propagate from outside the domain of the katabatic flow.

Bou-Zeid et al. (2020) provide a comprehensive survey of the impact of surface heterogeneity on the boundary layer, which directly generates horizontal variation of the surface wind field. The surface heterogeneity includes variability of land use (Pfister et al. 2017), sheltering by nearby higher vegetation and buildings, and local topography such as small depressions (Acevedo and Fitzjarrald 2003; Bodine et al. 2009; Medeiros and Fitzjarrald 2015; Guerra et al. 2018). Horizontal variations of soil and vegetation characteristics often induce significant horizontal variations in the nocturnal boundary layer, particularly in conditions of low wind speeds and clear skies (Van de Wiel et al. 2003; Stoll and Porté-Agel 2009). Chow et al. (2006) found that, in complex terrain, increasing model resolution was beneficial only if supported by high-resolution input for soil moisture. Acevedo et al. (2014) have emphasized that the nature of the submeso motions varies between sites partly due to surface heterogeneity and terrain.

Transient motions are often characterized by a horizontal length scale that is smaller than the observational network or grid area and thus can correspond to important horizontal variations of the observed wind field. Transient variations of the wind field include a wide variety of propagating submeso motions (Acevedo et al. 2014; Vercauteren et al. 2019). Such motions include microfronts and wind-direction shifts (Lang et al. 2018), internal gravity waves (Viana et al. 2010; Sun et al. 2015b), nearly horizontal two-dimensional modes (Anfossi et al. 2005; Mortarini et al. 2016; Cava et al. 2017; Stefanello et al. 2020), locally generated large-scale structures (Ansorge and Mellado 2014), longitudinal modes (Urbancic et al. 2020), and more complex modes. These motions may occur simultaneously and collectively perturb the local air flow and in thus induce turbulence that is intermittent and in non-equilibrium (e.g. Sun et al. 2015a; Vercauteren et al. 2016; Cava et al. 2019a; Mahrt 2020; Boyko and Vercauteren 2021). Kang et al. (2015) found that submeso motions can be classified into smooth structures, including wave-like motions that occur in less stable environments, sharper structures in more stable conditions, and step-like microfronts that occur in the most stable conditions. The vertical structure and transient inflection points in the wind profile partly determine the class of these motions. Vercauteren et al. (2019) found that wind-direction variability becomes large when the speed of the submeso motions become generally higher than the mean wind speed. The collective impact of coexisting different types of transient motions on the spatial variability of the wind field is not well understood and is site specific (Belušić and Mahrt 2008). Vercauteren et al. (2019) found strong site dependence for stable conditions when there was a scale separation between the submeso motions and the turbulence. Boyko

and Vercauteren (2021) examined the generation of intermittent turbulence by the submeso shear on time scales of 1 min to 1 hr in contrast to more stationary generation of turbulence by shear on larger time scales of 1–3 hrs. The submeso generation of intermittent turbulence depends on both height above ground and stability.

Compared to time variability, less is known about spatial variations of turbulence and submeso motions, the subject of this study. Investigation of the spatial variability of the wind field is partly motivated by the need to estimate the representativeness of observations of the wind vector at an individual measurement site towards the goal of inferring the wind vector for the surrounding area. Conversely, for an arbitrary point without observations, how representative is the nearest observation? Van den Bossche and De Wekker (2018) applied different methods for assessing the representativeness of one site with respect to a surrounding network of stations. Belušić and Mahrt (2008) evaluated a correlation length scale that describes the decrease of the correlation between two stations with increasing separation distance between them, using three networks over relatively flat terrain. For cases where the length scale is comparable to or less than the station spacing, the network does not function as a true network because the wind components between adjacent stations are weakly correlated (Staebler and Fitzjarrald 2004). Rigorous examination of interaction between submeso motions and surface heterogeneity/terrain is complex and benefits from detailed observations in the space−time domain (Pfister et al. 2019).

As additional motivation for the examination of local spatial variability of the wind field, numerical models partially resolve only those motions on horizontal scales greater than the width of the grid box and fully resolve only those motions on scales significantly larger than the grid box size. Motions on scales that are not large compared to the grid resolution are not resolved but may account for a significant fraction of the observed variability (Žagar et al. 2006). Statistical downscaling uses physically motivated corrections to map information from the resolved scale to smaller scales (Sheridan et al. 2018).

The unresolved subgrid motions generate turbulence and surface fluxes. Because such generation is not captured, the numerical model underestimates surface fluxes. Surface fluxes are often indirectly augmented by modifying the stability function, such as the long-tail distribution that allows significant turbulence for very large stability (Louis 1979). To predict non-vanishing scalar fluxes with vanishing resolved flow, Beljaars (1995), Fairall et al. (1996), Williams (2001), Edwards et al. (2020), and others considered a generalized velocity scale that includes a gustiness factor, which in convective conditions is related to w_* such that

$$V_{gen} \equiv \sqrt{V^2 + \beta w_*^2}. \tag{1}$$

This velocity scale replaces the resolved wind speed V in the bulk relation (Eq. 5 below). From a more general point of view, the convective velocity scale w_* can be replaced by a more general velocity scale, which represents all motions that are not resolved (Vickers and Esbensen 1998; Levy and Vickers 1999; Mahrt 2008). This generalization will form the basis for our analysis of the bulk formula, which concentrates on the stable nocturnal boundary layer.

We systematically examine the spatial variation of the nocturnal surface wind field on spatial scales of tens of metres to tens of kilometres by analyzing observations from eight different networks of surface observations. The goal is to identify a general measure of the small-scale variation of the wind field and its potential dependence on the wind speed and direction, stratification, topography, and network size and geometry.

2 Networks

We now summarize the basic characteristics of the networks. Additional details are listed in Table 1. The Shallow Cold Pool Experiment (SCP) is the primary dataset (Mahrt et al. 2014). The SCP experiment was conducted over semi-arid grasslands in north-east Colorado, USA, from 1 October to 1 December 2012. The main valley is relatively small, roughly 12 m deep and 270 m across. The width of the valley floor averages about 5 m with an average down-valley slope of about 2%, increasing to about 3% at the upper end of the valley. The side slopes of the valley are on the order of 10% or less. We analyze the 1-m sonic anemometer (CSAT3, Campbell Scientific) observations from 20 stations and from the main 30-m tower. The near-surface stratification is estimated from the NCAR hygrothermometers deployed at the 0.5- and 2-m levels at 19 of the stations.

The Dumosa dataset includes data from three short towers that form a triangle (Lang et al. 2018). Each station is 580 m from the centre (1160 m across the domain) and instrumented with Gill 2D sonic anemometers at 3 m. The site is flat (slope less than 0.03%) and is embedded within a larger region that is primarily flat. The dataset contains almost 2 years of data. The Pedras Altas network is embedded within a single slope with a typical slope value of 7.5%; the network elevation change is about 35 m, while the elevation change for the entire slope is about 70 m. The slope on the opposite side of the valley is significantly shorter with an elevation change of about 30 m. The network includes six stations with 034B Met-One cup anemometers and three stations with Väisälä WXT520 All-in-One at 2.5 m. Station 2 is eliminated because of missing data. Station 6 is the highest station and has the highest wind speeds. Some of the highest wind speeds were considered to be unlikely, and this station was also eliminated. Station 1 was located in a low-lying area with some surrounding bushes and characterized by the lowest wind speeds. This station is retained.

Results from CASES-19 (The Cooperative Atmospheric Surface Exchange Study) are reported because CASES-19 is historically an important dataset. However, CASES-19 includes only 4 weeks of data where all stations are reporting. The slope within the network was small. The CASES-19 network consisted of six short towers with Campbell Scientific CSAT3 anemometers deployed at 5 m. Station 3 was eliminated because of erratic behaviour. The Iowa network is characterized by field-scale heterogeneity, which is shown from remotely sensed information in Fig. 1 of Kustas et al. (2004). The surface elevation increases gradually to the west with a slope of less than 1% with embedded smaller scale variations of surface elevation. Three stations were deployed for a shorter duration over a small sub-area and are not used in this study, leaving nine stations with Campbell CSAT sonic anemometers at 2 m. The spacing between adjacent stations was highly variable because the station locations were chosen based on crop type.

The Perdigão network (Fernando et al. 2017) covers a deep valley defined by two relatively steep side slopes with variable surface vegetation. The network width is a little less than 2 km in the cross-valley direction, and the valley depth is about 175 m. Side slopes average about 20%. The network consists of 19 stations with CSAT sonic anemometers at 10 m. The variation of vegetation is substantial and complex. Because the Perdigão field program is dominated by ridge-top stations, we average measurements from the five ridge-top stations closest to the transect on the slope to form a single ridge-top measurement. We combine this ridge-top average with two valley stations and five stations on a side slope transect to form a subset of eight stations.

The Hudson Valley Ambient Meteorology Study (HVAMS) consisted of nine stations in a broad valley (Freedman and Fitzjarrald 2017). Station 7 was in a different topographi-

Table 1 Description of the networks

Site	sfc	wk	N	σ_{Zsfc}	τ	z	L_D	Citations
SCP	Grass	8	21	4.7	1	1	0.8	Mahrt et al. (2014)
CASES-99	Grass	4	7	3.0	1	5	0.5	Poulos et al. (2001)
DUMOSA	Grass	95	3	1.3	1	3	1.0	Lang et al. (2018)
Iowa	Crops	3	12	3	1	2	15	Kustas et al. (2004)
Pedras Altas	Mixed	8	10	10.0	2	2.5	0.95	Guerra et al. (2018)
Perdigão	Mixed	13	19	49	1	10	2	Fernando et al. (2017)
HVAMS	Mixed	9	7	14.2	5	7	65	Freedman and Fitzjarrald (2017)
FOG-82	Mixed	9	26	8	1	4	23	Acevedo and Fitzjarrald (2003)

Listed for each network are the surface type, the data duration (weeks), the number of stations (N), the standard deviation of the surface elevation that spans scales between 33 m and 1 km, σ_{Zsfc} (m), the averaging time τ (min) used to remove turbulence fluctuations (Eq. 2), the height of the sensors above ground, z (m), the domain width, L_D (km), and a citation with more information on the network

cal regime and was removed. Station 9 was removed because of significant missing data. Sheltering was important for some of the stations (Medeiros and Fitzjarrald 2015). FOG-82 (Acevedo and Fitzjarrald 2003) consisted of 26 stations with cup anemometers at 4 m. The network topography is complex, with multiple valleys and significant three-dimensionality of the topography.

We eliminated stations that are missing significant data or contain periods of erratic behaviour detected by quality control. For times when one or more stations are missing, we eliminated all station measurements for that time because some of the spatial quantities in our analyses are compromised with one or more stations missing. The station spacing must be suitably small so that correlations between adjacent stations are significant even for low wind speeds (Staebler and Fitzjarrald 2004). The networks in this study generally satisfy this criterion except for the very weakest winds. The networks capture motions on scales smaller than the domain width L_D (Table 1) and larger than the station spacing. The station spacing is inversely related to the number of stations (N, Table 1). Determination of L_D is somewhat ambiguous, particularly with networks that have irregular shapes; here, L_D is computed in terms of the length of the major (longest) axis of the domain.

2.1 Defining Nocturnal

We define the nocturnal period to be from 2100 to 0600 local standard time (LST = UTC + 6) in an effort to exclude the complex transition periods (Angevine et al. 2020). We have examined the sensitivity to the choice of these selection times. The results were at least qualitatively similar, and the conservative fixed times independent of season are used here to make the results more easily reproducible by others. We have previously used time limits that varied daily based on the local sunset and sunrise times, and results were qualitatively the same except that the fixed times unnecessarily lose some data during the longer nocturnal periods in the winter season.

2.2 Quantification of Network Topography

The variability of the terrain is represented by the standard deviation of the digitized surface elevation, σ_{Zsfc}, based on the Global Multi-Resolution Terrain Elevation Data 2010

(GMTED2010) documented in Danielson and Gesch (2011). To estimate the effect of resolution, we analyze data at the highest available resolution (7.5 arc-seconds, approximately 250-m pixel size) and the lowest resolution (30 arc-seconds, approximately 1-km pixel size). Because these GMTED2010 data were produced using 1-arc-second input data (33-m resolution), it offers statistical measures characterizing the terrain at each output pixel, such as mean, median, and standard deviation. The value of σ_{Zsfc} for the network is calculated as the within-pixel standard deviation averaged over all the pixels in the network. This is done separately for both the 250-m and 1-km GMTED2010 pixel resolutions, resulting in network-averaged standard deviations for spatial scales between 33 and 250 m and between 33 m and 1 km.

The network boundaries are defined by the outermost stations. This results in a rectangular domain, which is appropriate for calculating σ_{Zsfc} for the majority of networks but could include unrelated terrain for diagonally elongated networks. Additionally, standard deviation of the GMTED2010-resolved terrain can be calculated using the mean terrain height at each pixel of the network, which estimates the terrain variation on scales between the pixel scale (250 m or 1 km) and the scale of the network. This standard deviation can be added to the within-pixel σ_{Zsfc} to estimate the total terrain standard deviation of the network, which is briefly discussed in Sect. 5.3.

2.3 Partitioning

Space−time decompositions and averaging can be carried out in a number of different ways. Here, we begin with the time decomposition at a fixed point and then incorporate spatial averaging. We pursue a relatively simple approach. The local time averaging is written as

$$\phi = \phi' + \overline{\phi}, \tag{2}$$

where ϕ is the potential temperature or one of the velocity components and $\overline{\phi}$ is the average over the time interval τ. ϕ' is the deviation from a local time average and is ideally dominated by turbulent fluctuations. The averaging time τ for each field program is listed in Table 1.

The wind speed is then calculated as

$$U \equiv \sqrt{\overline{u}^2 + \overline{v}^2}, \tag{3}$$

where the wind components $\overline{u}$ and $\overline{v}$ are the eastward and northward components (no rotation has been applied). Submeso motions in the stable boundary layer on scales just larger than the turbulence are normally defined in the time domain, and more information is needed in terms of spatial scales. The spatial domain can be posed in terms of an observational network or grid area of a numerical model. For submeso motions, there is not a known relationship between the space and time scales.

The spatial average is written as $\langle\phi\rangle$ where the angle brackets indicate spatial averaging. The above quantities will sometimes also be averaged over intervals (bin averaging) of the wind speed. This bin averaging is indicated by square brackets, such as $[\phi]$. Only bins that include 20 or more samples are retained. The standard error bars are often small because of the large sample size. However, the standard error probably seriously underestimates the actual sampling error because the samples are not independent due to the non-stationarity. Bin averages based on spatially-averaged variables are written as $[\langle\phi\rangle]$.

2.4 Spatial Averaging of the Wind Vector

Consider two versions of the spatially-averaged wind. The speed of the vector average wind is written as

$$\langle V\rangle \equiv (\langle u\rangle^2 + \langle v\rangle^2)^{0.5}. \tag{4}$$

The wind speed predicted by a numerical model for a grid area can be identified with $\langle V\rangle$. The area-averaged wind speed will be written as $\langle U\rangle$. The speed of the vector average, $\langle V\rangle$, is smaller than the scalar spatial average $\langle U\rangle$. We define V_{sm} such that

$$\langle U\rangle^2 \equiv \langle V\rangle^2 + V_{sm}^2, \tag{5}$$

where V_{sm} accounts for the spatial variability of the wind speed that is not resolved by the calculation of $\langle V\rangle$ based on the vector-averaged wind. In the limit where the spatial variability of the wind vector vanishes, V_{sm} vanishes. In the other limit of random wind direction, the speed of the resolved vector-averaged wind is zero.

An alternative measure of variation of the wind vector within a network can be defined as (Mahrt 2007; Van den Bossche and De Wekker 2018)

$$\sigma_V \equiv \sqrt{\sigma_u^2 + \sigma_v^2}, \tag{6}$$

where σ_u and σ_v are the standard deviations of the spatial variation of the wind components $\overline{u}$ and $\overline{v}$. Here, σ_V is well correlated to V_{sm} and shows similar dependence on $\langle V\rangle$. It can be shown that in the limit of small V_{sm}, V_{sm} numerically approaches σ_V. We arbitrarily proceed using only V_{sm}.

3 An Example: The Transfer Coefficient for Heat

The next two sections concentrate on the measurements from the SCP network, which is the most complete dataset and includes quality measurements of the stratification at the flux stations. The SCP network is over simple terrain dominated by a single shallow valley and provides an opportunity to understand the impact of the terrain. Beginning in Sect. 5, we compare all of the networks.

We now introduce a bulk relation for the heat flux at a fixed point and then extend this to spatially-averaged flow. For a fixed point,

$$\overline{w'\theta'} \equiv -C_H U \delta_z \theta, \tag{7}$$

where C_H is a transfer coefficient and $\delta_z\theta$ is the vertical difference of potential temperature between two observational levels. Note that C_H in Eq. 7 approximates the eddy transfer coefficient for heat. For our analysis of the observations,

$$\delta_z\theta \equiv \overline{\theta}(z2) - \overline{\theta}(z1), \tag{8}$$

where $z1$ and $z2$ identify two observational levels near the surface, 0.5 m and 2 m for the SCP measurements.

The area-averaged fluxes require information of the spatial variability of the local wind speed to compute the area-averaged wind speed $\langle U\rangle$. We assume that the turbulence maintains equilibrium with the local wind. The bulk relation for the spatially-averaged heat flux is then written as

$$\langle\overline{w'\theta'}\rangle \equiv -\langle C_H\rangle\langle U\rangle\langle\delta_z\theta\rangle. \tag{9}$$

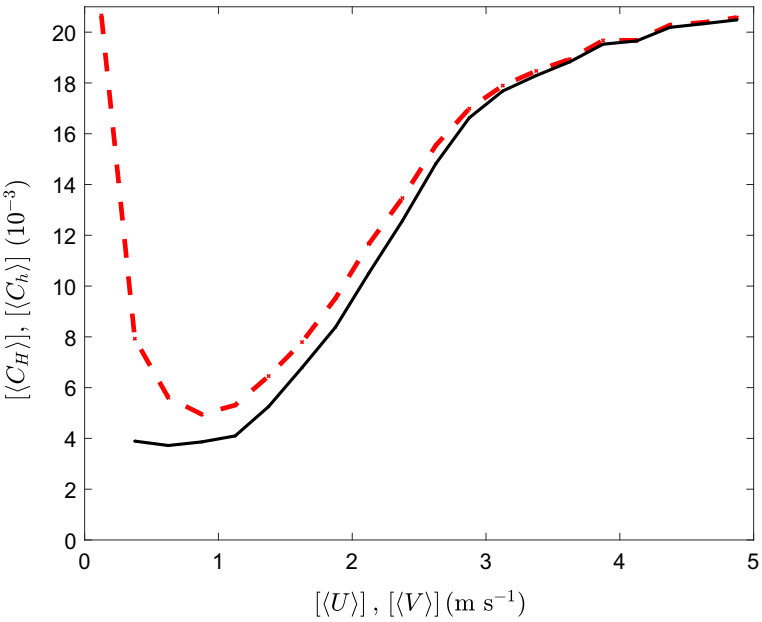

Fig. 1 For the SCP network, $[\langle C_h \rangle]$, based on the magnitude of the spatially-averaged wind vector $[\langle V \rangle]$ and the spatially-averaged heat flux (Eq. 12), is plotted as a function of $[\langle U \rangle]]$ (dashed curve). $[\langle C_H \rangle]$ (Eq. 11) based on the magnitude of the spatially-averaged wind speed $[\langle U \rangle]]$ and the spatially-averaged heat flux is plotted as a function of $[\langle U \rangle]]$ (solid curve)

$\langle C_H \rangle$ is not a spatial average of C_H, but rather computed from the spatial averages on the right-hand side of Eq. 9.

Recall that bin-averaged products and ratios are computed by first bin averaging individual variables. For example, the transfer coefficient for heat is written as

$$[C_H] \equiv \frac{[\overline{w'\theta'}]}{[U][\delta_z \theta]}, \tag{10}$$

or starting with spatial averages, we define

$$[\langle C_H \rangle] \equiv \frac{[\langle \overline{w'\theta'} \rangle]}{[\langle U \rangle][\langle \delta_z \theta \rangle]}. \tag{11}$$

This definition of the transfer coefficient includes the effect of the spatial variation of the wind speed.

Using winds that are vector-averaged over an area, we also define

$$[\langle C_h \rangle] \equiv \frac{[\langle \overline{w'\theta'} \rangle]}{[\langle V \rangle][\langle \delta_z \theta \rangle]}. \tag{12}$$

Because the speed of the vector-averaged wind for low wind speeds is often much less than the spatially-averaged wind speed, $[\langle C_h \rangle]$ may require very large values for low wind speeds in order to the predict the correct heat flux.

For the SCP measurements, $[\langle C_h \rangle]$ based on the observed $\langle V \rangle$ becomes large for small $\langle V \rangle$ (dashed curve, Fig. 1) because of the omission of flux generation by the sub-domain variability of wind speed. Then, $[\langle C_H \rangle]$ based on the spatially-averaged wind speed $\langle U \rangle$ (solid,

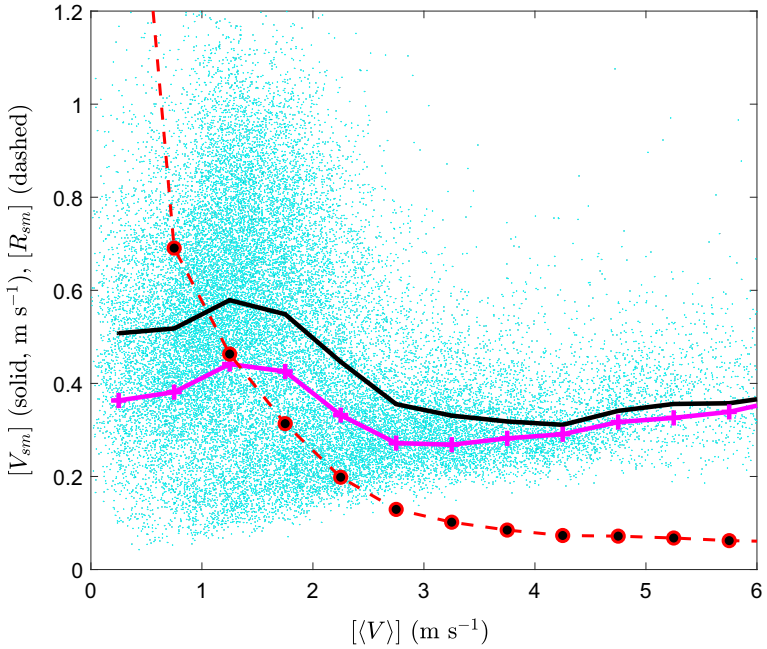

Fig. 2 **a** $[V_{sm}]$ (Eq. 5) as a function of the speed of the vector-averaged wind $[\langle V\rangle]$ (black curve) for the SCP network and for 5 stations in the valley (magenta curve with X's). Individual values of V_{sm} are shown with cyan dots. The ratio of $[V_{sm}]$ to $[\langle V\rangle]$ (R_{sm}, Eq. 13) is shown as a function of the speed of the vector-averaged wind $[\langle V\rangle]$ (red dashed)

Fig. 1) does not increase for small $\langle U\rangle$, because it includes the sub-domain generation of the turbulence and associated heat flux. A formulation of V_{sm} (Eq. 5) based on the observational analyses can be used to predict $[\langle U\rangle]$ from the model-produced $[\langle V\rangle]$, an eventual goal of this work.

The transfer coefficient for heat is expected to be related to stability, not included in Fig. 1. However, the stratification cannot be confidently evaluated in a systematic way for most of the networks. Often the stratification is not available or the measurements of the stratification are difficult to interpret because of complex vegetation. In general, the stratification is inversely related to the wind speed so that the wind speed serves as a reasonable overall forcing variable. However, the relationship between the stratification and the wind speed can be influenced by even weak topography (Lapworth and Osborne 2020). The transfer coefficient for the heat flux could be examined as a function of z/L where L is the Obukhov length, which requires only information on the turbulent fluxes. However, self-correlation is most important for very stable conditions, the emphasis of our study. The HOckey-Stick Transition (HOST) formulation (Sun et al. 2020; Grisogono et al. 2020) avoids this self-correlation and better describes a commonly observed fundamental transition between low-wind-speed and high-wind-speed conditions, although this approach has been explored primarily for the momentum flux and is outside the scope of this study.

4 Dependence on Wind Speed

For the SCP network, $[V_{sm}]$ reaches a peak of 0.6 m s^{-1} for 1 m s^{-1} $< [\langle V \rangle] <$ 2 m s^{-1} (Fig. 2, black solid). This peak is partly associated with local katabatic flows and cold pools. Also, $[V_{sm}]$ reaches a minimum at about $[\langle V \rangle] \approx 4$ m s^{-1} and then increases very slowly with further increases of $[\langle V \rangle]$. The latter is partly related to greater impact of the topography and lee turbulence when the northerly flow component (cross valley) becomes significant. The scatter is large, as visualized by the individual 1-min observations of V_{sm} (cyan dots). For five stations on the valley floor (magenta curve), $[V_{sm}]$ is smaller for low wind speeds when the valley floor is often within a cold pool. For higher wind speeds, V_{sm} for the valley stations becomes similar to that for the entire network.

The ratio

$$R_{sm} \equiv \frac{[V_{sm}]}{[\langle V \rangle]} \tag{13}$$

represents the relative importance of spatial variations of the wind within the network. When R_{sm} approaches values small compared to unity, an individual station is representative of the entire network. The area of representativeness of an individual station generally decreases with increasing R_{sm}. As R_{sm} becomes large compared to unity, even adjacent stations may be poorly correlated. R_{sm} decreases rapidly with increasing $[\langle V \rangle]$ from $R_{sm} > 2$ (offscale) for $[\langle V \rangle] < 0.5$ m s^{-1} to $R_{sm} < 0.2$ for $[\langle V \rangle] > 2$ m s^{-1} (Fig. 2a, red dashed). Our primary interest is in low-wind conditions.

4.1 Bivariate Distribution

Using bivariate analysis (Williams et al. 2013), we briefly examine the simultaneous dependence of V_{sm} on $\langle V \rangle$ and $\langle \delta_z \theta \rangle$ for the SCP network (Fig. 3) where accurate measurements of the stratification are available for each station. The wind speed V_{sm} reaches maximum values for $\langle V \rangle$ of 1–2 m s^{-1} for $\delta_z \theta > 0.7$ K, where V_{sm} is above 0.55 m s^{-1}. For significant stratification, V_{sm} does not depend on the exact value of stratification. This regime corresponds to well-defined cold pools, down-valley flow, and side-slope katabatic flows. These features lead to large variation of the wind vector across the observational network. The increase of V_{sm} with increasing stratification is opposite to the decrease of turbulence with increasing stratification. Reduced turbulence and corresponding reduced vertical coupling is more conducive to development of horizontal gradients of the wind speed.

For low wind speeds and $\delta_z \theta < 0.5$ K, V_{sm} averages less than 0.5 m s^{-1}. These conditions include numerous cloudy or partly cloudy cases. With clear skies, katabatic flows down the side slopes and down the valley increase V_{sm} and contribute to $\langle V \rangle$ such that $\langle V \rangle$ generally becomes > 1 m s^{-1}. For small $\delta_z \theta$ along the bottom of the graph, V_{sm} increases gradually with increasing $\langle V \rangle$. Significant winds over the topography with small stratification induce substantial spatial variation of the wind vector. This is partly due to lee turbulence in spite of the low amplitude of the topography (Mahrt 2017). For higher wind speeds, the greater mixing generally reduces the stratification. The exact details shown in Fig. 3 are influenced by the interpolation scheme.

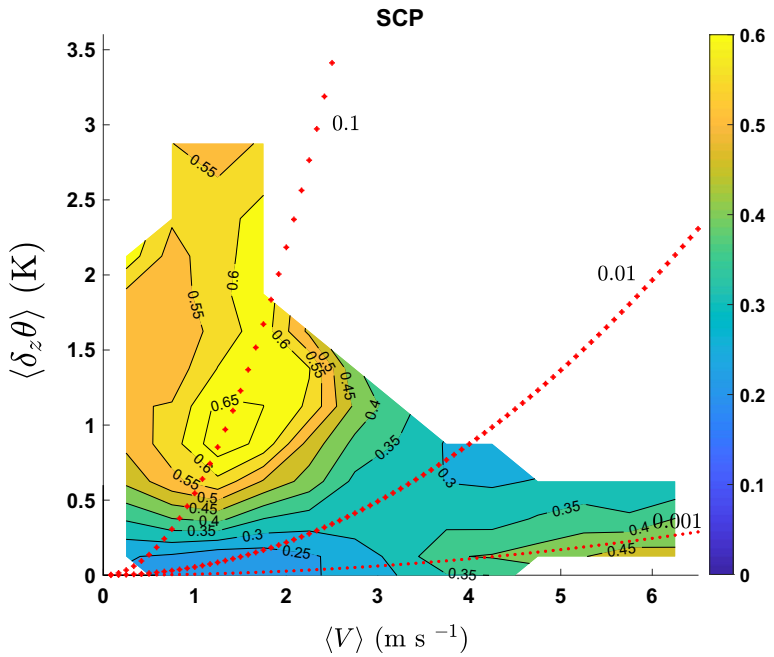

Fig. 3 The dependence of V_{sm} on $\langle V \rangle$ and $\langle \delta_z \theta \rangle$ for the SCP site. Red dashed curves correspond to constant values of the surface-layer Richardson number (Eq. 14)

4.2 Stability

The red curves in Fig. 3 represent constant values of the surface-layer Richardson number

$$Rb \equiv \frac{gz\langle \delta_z \theta \rangle}{\Theta \langle U \rangle^2}, \tag{14}$$

which is computed from the spatially-averaged 1-m wind speed and from the spatially-averaged potential temperature at the 0.5- and 2-m levels.

The dotted red curve corresponding to $Rb = 0.1$ passes through the region of maximum V_{sm} (Fig. 3). Notice that this line is approximately perpendicular to the curves of constant V_{sm}, indicating that Rb is a poor predictor of V_{sm}. The quantity V_{sm} generally increases with increasing stratification, but V_{sm} is either relatively independent of $\langle V \rangle$ or increases with $\langle V \rangle$, depending on the network (Fig. 4, Sect. 5). That is, the dependence of V_{sm} on Rb through variations of $\langle V \rangle$ opposes the dependence of V_{sm} on Rb through variations of stratification. The poor relationship between V_{sm} on Rb may also be due to generation of propagating submeso motions at a distant location far from the observational site. In the statically unstable case, the dependence of V_{sm} on $\langle V \rangle$ and the stratification is more complex (not shown), perhaps due to the influence of the boundary-layer depth and frequent occurrence of a number of different regimes of very large eddies/mesoscale motions (Salesky and Anderson 2018, 2020; Katul 2019).

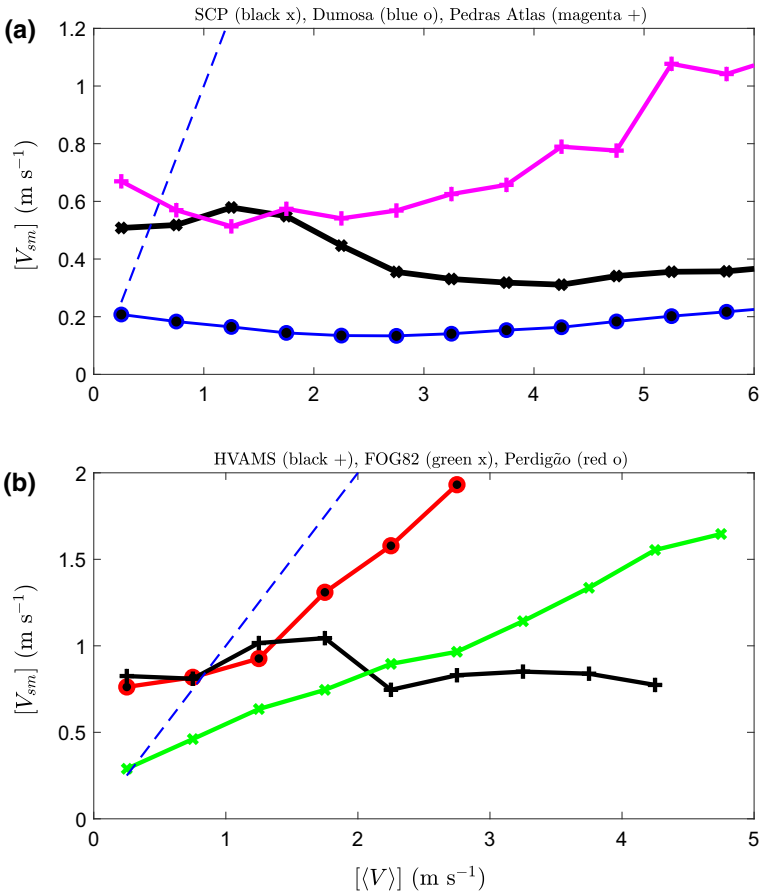

Fig. 4 $[V_{sm}]$ (Eq. 5) as a function of the speed of the vector-averaged wind $[\langle V \rangle]$ for **a** the small networks and **b** the large networks. The one-to-one relationship is shown by the blue dashed line

5 Comparison Between Networks

We now examine the dependence of $[V_{sm}]$ on $[\langle V \rangle]$ for the other networks. The CASES-19 and Iowa networks are excluded from this analysis because the sample sizes are too small to confidently capture the dependence of $[V_{sm}]$ on wind speed. The CASES-19 and Iowa networks are restored in the subsequent analysis, which does not require a large sample size. The dependence of $[V_{sm}]$ on $[\langle V \rangle]$ for the SCP network (Fig. 4a, black $\times$) is discussed above based on Fig. 2. The wind speed $[V_{sm}]$ is quite small for the Dumosa site (Fig. 4a, blue O), averaging only about 0.2 m s^{-1}. The Dumosa site is flat and embedded within a larger region of relatively flat homogeneous terrain. $[V_{sm}]$ increases with increasing $[\langle V \rangle]$ for the Pedras Altas network (Fig. 4a, magenta +). The Pedras Altas network is located entirely on a single slope (approximately 7.5%), and the wind speeds at the upper part of the network increase more rapidly with increasing $[\langle V \rangle]$ compared to wind speeds on the lower part of the slope, which in turn increases $[V_{sm}]$.

The wind speed $[V_{sm}]$ is large for the Perdigão network (Fig. 4b, red circle) where the weak flow on the valley floor remains decoupled from the ridge top flow even for the more

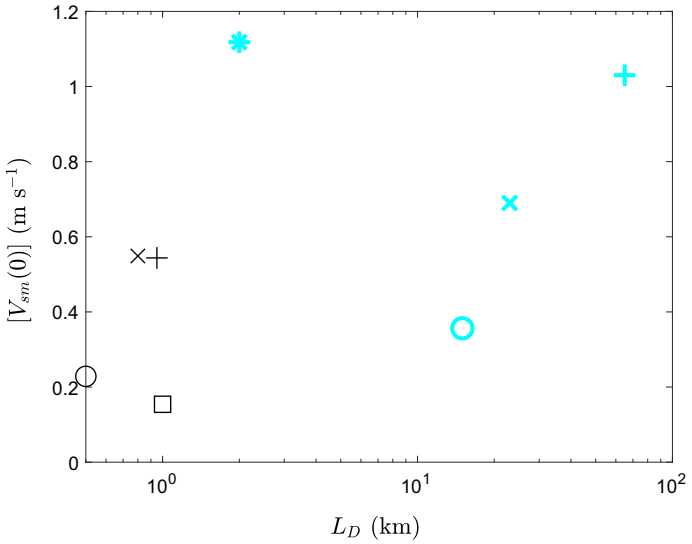

Fig. 5 The values of $[V_{sm}(0)]$ as a function of the network size, L_D, for the SCP (black ×), CASES99 (black O), Pedras Altas (black +), Dumosa (black square), Iowa (cyan O), Perdigão (cyan asterisk), HVAMS (cyan +), and FOG-82 (cyan ×) networks. Networks with domain size $L_D \leq 1$ km are indicated with black symbols and $L_D \geq 1$ km with cyan symbols

significant wind speeds. As $[\langle V \rangle]$ increases, the ridge-top wind speeds increase while the wind speed on the valley floor does not appreciably increase. Recirculation in the lee of the ridge (Menke et al. 2019) also contributes to the wind speed $[V_{sm}]$. Finally, the similarity of the dependence of $[V_{sm}]$ on $[\langle V \rangle]$ for the HVAMS network (Fig. 4b, black +) compared to that for the SCP site (Fig. 4a, black x) is probably fortuitous.

5.1 Low Wind Speeds

In general, $[V_{sm}]$ is significant compared to $[\langle V \rangle]$ when $[\langle V \rangle] < 2$ m s^{-1}. Theoretically, we define $[V_{sm}(0)]$ as the expected value of $[V_{sm}]$ as $[\langle V \rangle]$ vanishes. We can pragmatically estimate $[V_{sm}(0)]$ from measurements for low wind speeds. Some networks include cup anemometers, which do not capture the wind field when the wind speed is less than an instrumental threshold value. We can estimate $[V_{sm}(0)]$, for example, in terms of 1 m s^{-1} $< [\langle V \rangle] < 2$ m s^{-1}. This procedure relies on the fact that $[V_{sm}]$ for low wind speeds usually varies only slowly with increasing wind speed so that 1 m s^{-1} $< [\langle V \rangle] < 2$ m s^{-1} generally serves as a useful estimate of $[V_{sm}(0)]$. The dependence of $[V_{sm}(0)]$ on terrain (Sect. 5.3) is more predictable when based on 1 m s^{-1} $< [\langle V \rangle] < 2$ m s^{-1}, than when based on $[\langle V \rangle] <$ 1 m s^{-1}.

5.2 Dependence on Network Size

By definition, $[V_{sm}(0)]$ must vanish as the network size, L_D, vanishes. Larger networks capture a larger range of submeso variations. Nonetheless, the dependence of $[V_{sm}(0)]$ on network size is generally weak (Fig. 5). The wind speed $[V_{sm}(0)]$ increases approximately

linearly with L_D for the three largest networks although it is not known if this result is significant or spurious. The values of $[V_{sm}](0)$ are quite large for the Perdigão site in spite of the modest size (Fig. 5, cyan asterisk). The Perdigão network covers a relatively deep valley with steep side slopes (approximately 20%). The wind speed $[V_{sm}(0)]$ for the Iowa network (cyan circle) is small considering the larger domain size, and is quite small for the flat Dumosa network (black square). Amongst the different networks, the influence of minimum station spacing within the network was of little predictive value, the average station spacing was of modest value, and the maximum station spacing was closely related to the domain size.

The relative insensitivity to the domain size contrasts with studies over the sea based on aircraft measurements (Vickers and Esbensen 1998) or incorporated satellite data (Levy and Vickers 1999) where a version of $[V_{sm}]$ was evaluated. Over the sea, $[V_{sm}]$ was clearly proportional to the size of the spatial domain, although the sample size was relatively small. It is not known if the dependence on size of the spatial domain would emerge as the leading factor for networks over a flat homogeneous land surface. The failure of L_D to explain much of the variation of $[V_{sm}(0)]$ for the current datasets motivates exploring the influence of topography on $[V_{sm}(0)]$.

5.3 Dependence on Topography

We now examine the dependence of $[V_{sm}(0)]$ on the topography as represented by the standard deviation of the digitized terrain, σ_{Zsfc} (Sect. 2.2). $[V_{sm}(0)]$ is shown as a function of σ_{Zsfc} based on horizontal scales between 33 m and 250 m (Fig. 6a) and based on scales between 33 m and 1 km (Fig. 6b). For a given value of σ_{Zsfc}, $[V_{sm}(0)]$ for network sizes $\leq$ 1 km tends to be a little smaller than $[V_{sm}(0)]$ for network sizes $\geq$ 1 km, although the significance of this difference is unknown. The wind speed $[V_{sm}(0)]$ for the Perdigão network deviates significantly from the trend for the 250-m pixel size (cyan asterisk, Fig. 6a), but more closely follows the trend for the 1-km pixel size (cyan asterisk, Fig. 6b), indicating that variability of terrain on scales between 250 m and 1 km is important. However, including the terrain variation on scales between 1 km and the domain size (when $L_D > 1$ km) slightly degrades the relationship between $[V_{sm}(0)]$ and σ_{Zsfc} (not shown), indicating that the larger-scale terrain for these particular networks does not effectively generate sub-domain motions. Representation of the terrain with a single quantity is difficult because the terrain is characterized not only by the horizontal scale, but also by the geometry of the terrain (ridges, valleys, basins, and smaller three-dimensional features).

As an example, a subjective fit for $[V_{sm}(0)]$ based on the 1-km pixels can be written as (Fig. 6b, solid curve)

$$[V_{sm}(0)] = 1.5(\sigma_{Zsfc}/50)^{0.5}. \tag{15}$$

Because of the sensitivity of σ_{Zsfc} to the range of scales included in the calculation of σ_{Zsfc}, a more formal regression analysis with goodness of fit is not justified. Equation 15 can be used to predict the ratio $R_{sm} \equiv [V_{sm}]/[\langle V \rangle]$ (Eq. 13). As the terrain increases, the stations become less representative of their surrounding area.

These results indicate that $[V_{sm}(0)]$ depends significantly on the terrain (Fig. 6b). However, we also find that combining information on σ_{Zsfc} and L_D improves the prediction of $[V_{sm}(0)]$ in spite of the weak dependence of $[V_{sm}(0)]$ on L_D alone (Fig. 5). Consider the following short exercise, which could serve as a motivation for future analyses with more networks. Figure 6c shows $[V_{sm}(0)]$ as a function of σ_{Zsfc} and L_D by replacing σ_{Zsfc} with the expression

$$G(\sigma_{Zsfc}, L_D) = \sigma_{Zsfc} + L_D/C, \tag{16}$$

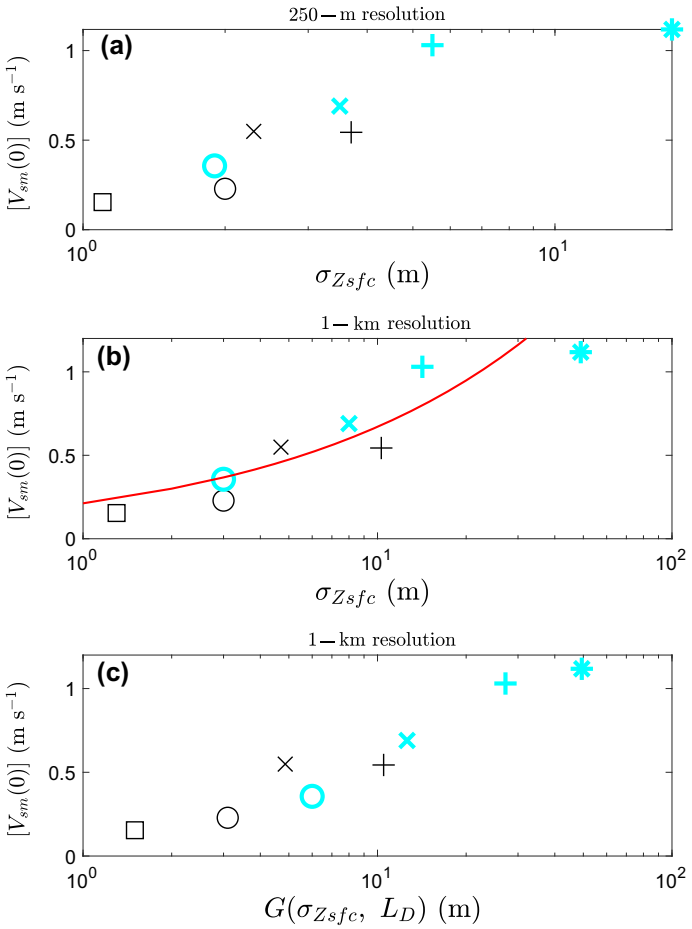

Fig. 6 The values of $[V_{sm}(0)]$ as a function of σ_{Zsfc} based on digitized terrain for scales **a** between 33 m and 250 m and **b** between 33 m and 1 km where the red solid curve is Eq. 15. **c** The values of $[V_{sm}(0)]$ as a function of $G(\sigma_{Zsfc}, L_D)$ defined by Eq. 16 where σ_{Zsfc} is based on scales between 33 m and 1 km. The networks are SCP (black x), CASES-99 (black O), Pedras Altas (black +), Dumosa (black square), Iowa (cyan O), Perdigão (cyan asterisk), HVAMS (cyan +), and FOG-82 (cyan x). Networks with domain size $L_D \leq 1$ km are indicated with black symbols and $L_D \geq 1$ km with cyan symbols

where σ_{Zsfc} and L_D are in metres and $C = 5000$ is chosen as a subjective fit. This relation appears to improve the representation of $[V_{sm}(0)]$. Because the number of points is limited and the values of $[V_{sm}(0)]$ for each network are influenced by details of the instrumentation deployment, formal fitting of Fig. 6c seems not justified. Inclusion of the limiting case where $[V_{sm}(0)]$ should vanish when L_D vanishes requires additional complexity.

We summarize the above results in terms of the bulk relation by combining Eqs. 5 and 9 to obtain

$$\langle \overline{w'\theta'} \rangle \equiv -\langle C_H \rangle \sqrt{\langle V \rangle^2 + V_{sm}(0)^2}\ \langle \delta_z \theta \rangle. \tag{17}$$

Recall that as $\langle V \rangle$ exceeds roughly 2 m s^{-1}, $V_{sm}(0)$ quickly becomes unimportant. An estimate of $V_{sm}(0)$ can be made using Eq. 15, for example, or simply specified as a constant,

such as 0.5 m s^{-1}, which improves upon completely neglecting $[V_{sm}(0)]$ in the bulk relation. With vanishing resolved wind speed, the heat flux becomes $\langle C_H \rangle V_{sm}(0) \langle \delta_z \theta \rangle$. Application of Eq. 17 must recognize the complexity of the problem and the unknown compatibility of Eq. 17 with other components of a potential host model and historical adjustment of the associated model coefficients. As a sensitivity study, does the incorporation of Eq. 17 into the host model significantly change the prediction of the heat flux by the host model?

6 Conclusions

We examined the spatial variability of the nocturnal wind field using eight networks of surface observations and focused on analysis of $V_{sm}^2 \equiv \langle U \rangle^2 - \langle V \rangle^2$. The spatially-averaged wind speed $\langle U \rangle$ is larger than the speed of the vector-averaged wind $\langle V \rangle$ due to the spatial variability of the wind field within the network (V_{sm}). The spatially-averaged heat flux is directly related to $\langle U \rangle$, not the smaller $\langle V \rangle$. However, the bulk relation in a numerical model must relate the grid-averaged heat flux to the speed of the grid-resolved flow $\langle V \rangle$ and thus can significantly underestimate the heat flux at low wind speeds. Here, the bulk relation has been modified through a generalized velocity scale that includes V_{sm} to estimate the needed $\langle U \rangle$.

Additional applications of V_{sm} include assessment of the potential uncertainty of estimating the wind at an arbitrary fixed point from nearby wind observations. Wind observations at a fixed point are representative of a greater surrounding area when the wind speed increases.

The small-scale variability of the wind (V_{sm}) was contrasted between the networks in terms of the wind speed, the wind direction, and the topography. The standard deviation of the surface elevation accounts for much of the between-network variation of V_{sm} (Sect. 5.3). The size of the network seems to be of secondary importance for the current datasets. Local topography on scales smaller than the network can be important through local generation of katabatic flows, cold pools, and lee turbulence. Significant spatial variability of the wind field can also be generated by transient submeso motions such as propagating wave-like modes, which are often related to distant topography. Submeso motions, and thus V_{sm}, tend to increase with increasing stratification in contrast to the turbulence, which decreases with increasing stratification. Section 5.3 uses information from the eight networks to predict V_{sm}, although the generality of this prediction is unknown and more work is required.

Future networks should use only sonic anemometers and not cup anemometers to avoid threshold problems at low wind speeds where V_{sm} is most important. Accurate temperature measurements at two or more levels would be required to estimate the stratification. A network over a flat homogeneous surface could serve as a useful baseline.

Acknowledgements We gratefully acknowledge the important comments of Luca Mortarini, Branko Grisogono, Joan Cuxart, and an anonymous reviewer. Larry Mahrt is funded by Grant AGS 1945587 from the U.S. National Science Foundation. Otávio Acevedo is supported by the Brazilian Conselho Nacional de Desenvolvimento Cientifico e Tecnológico (CNPq) and the Comissão de Aperfeiçoamento de Pessoal de Ensino Superior (CAPES). We gratefully acknowledge Dave Fitzjarrald for the HVAMS and FOG-82 data and assistance in use of the measurements. The data from the Perdigão group, accessed via https://www.eol.ucar.edu/field_projects/Perdigão, are gratefully acknowledged. The Earth Observing Laboratory of the National Center for Atmospheric Research provided the SCP and CASES-99 measurements. We also wish to acknowledge William Kustas and John Preuger for the Iowa data.

References

Abraham C, Monahan A (2020) Spatial dependence of stably stratified nocturnal boundary-layer regimes in complex terrain. Boundary-Layer Meteorol 177:19–47

Acevedo O, Fitzjarrald D (2003) In the core of the night—effect of intermittent mixing on a horizontally heterogeneous surface. Boundary-Layer Meteorol 106:1–33

Acevedo O, Costa F, Oliveira P, Puhales F, Degrazia G, Roberti D (2014) The influence of submeso processes on stable boundary layer similarity relationships. J Atmos Sci 71:207–225

Anfossi D, Oetti D, Degrazia G, Boulart A (2005) An analysis of sonic anemometer observations in low wind speed conditions. Boundary-Layer Meteorol 114:179–203

Angevine W, Edwards JM, Lothon M, LeMone MA, Osborne SR (2020) Transition periods in the diurnally-varying atmospheric boundary layer over land. Boundary-Layer Meteorol 177:205–223

Ansorge C, Mellado J (2014) Global intermittency and collapsing turbulence in a stratified planetary boundary layer. Boundary-Layer Meteorol 153:89–116

Banta R, Pichugina Y, Newsom R (2003) Relationship between low-level jet properties and turbulence kinetic energy in the nocturnal stable boundary layer. J Atmos Sci 60:2549–2555

Beljaars A (1995) The parameterization of surface fluxes in large-scale models under free convection. Q J R Meteorol Soc 121:255–270

Belušić D, Mahrt L (2008) Estimation of length scales from mesoscale networks. Tellus 60a:706–715

Bodine D, Klein P, Arms S, Shapiro A (2009) Variability of surface air temperature over gently sloped terrain. J Appl Meteorol 48:1117–1141

Bou-Zeid E, Anderson W, Katul GG, Mahrt L (2020) The persistent challenge of surface heterogeneity in boundary-layer meteorology: a review. Boundary-Layer Meteorol 177:227–245

Boyko V, Vercauteren N (2021) Multiscale shear forcing of turbulence in the nocturnal boundary layer: a statistical analysis. Boundary-Layer Meteorol 179:43–72

Cava D, Mortarini L, Giostra U, Richiardone R, Anfossi D (2017) A wavelet analysis of low wind speed submeso motions in a nocturnal boundary layer. Q J R Meteorol Soc 143:661–669

Cava D, Mortarini L, Anfossi D, Giostra U (2019a) Interaction of submeso motions in the Antarctic stable boundary layer. Boundary-Layer Meteorol 171:151–173

Cava D, Mortarini L, Giostra U, Acevedo O, Katul G (2019b) Submeso motions and intermittent turbulence across a nocturnal low-level jet: a self-organized criticality analogy. Boundary-Layer Meteorol 172:17–43

Chow F, Weigel A, Street R, Rotach M, Xue M (2006) High-resolution large-eddy simulations of flow in a steep alpine valley. Part I: methodology, verification, and sensitivity studies. J Appl Meteorol Climatol 45:63–68

Cuxart J (2008) Nocturnal basin low-level jets: an integrated study. Ann Geophys 56:100–113

Cuxart J, Jiménez M, Martínez D (2007) Nocturnal mesobeta basin and katabatic flows on a midlatitude island. Mon Weather Rev 135:918–932

Cuxart J, Cunillera J, Jiménez MA, Martínez D, Molinos F, Palau JL (2012) Study of mesobeta basin flows by remote sensing. Boundary-Layer Meteorol 143:143–158

Cuxart J, Martínez-Villagrasa D, Stiperski I (2020) Validation of a simple diagnostic relationship for downslope flows. Atmos Sci Lett. https://doi.org/10.1002/asl.965

Danielson J, Gesch D (2011) Global multi-resolution terrain elevation data 2010 (GMTED2010). Geological Survey, Tech rep, U.S. https://doi.org/10.3133/ofr20111073

Edwards J, Beljaars ACM, Holtslag AAM, Lock AP (2020) Representation of boundary-layer processes in numerical weather prediction and climate models. Boundary-Layer Meteorol 177:511–539

Fairall C, Bradley E, Rogers D, Edson J (1996) Bulk parameterization of air-sea fluxes for tropical ocean-global atmosphere coupled-ocean atmosphere response experiment. J Geophys Res 101:3747–3764

Fedorovich E, Shapiro A (2009) Structure of numerically simulated katabatic and anabatic flows along steep slopes. Ann Geophys 57:981–1010

Fedorovich E, Shapiro A (2017) Oscillations in Prandtl slope flow started from rest. Q J R Meteorol Soc 143:670–677

Fernando HJS, Mann J, Palma JMLM, Lundquist JK, Barthelmie RJ, Belo-Pereira M, Brown WOJ, Chow FK, Gerz T, Hocut CM, Klein PM, Leo LS, Matos JC, Oncley SP, Pryor SC, Bariteau L, Bell TM, Bodini N, Carney MB, Courtney MS, Creegan ED, Dimitrova R, Gomes S, Hagen M, Hyde JO, Kigle S, Krishnamurthy R, Lopes JC, Mazzaro L, Neher JMT, Menke R, Murphy P, Oswald L, Otarola-Bustos S, Pattantyus AK, Veiga CRA, Schady Sirin N, Spuler S, Svensson E, Tomaszewski J, Turner DD, van Veen L, Vasiljevi N, Vassallo D, Voss S, Wildmann N, Wang Y (2017) The Perdigão: peering into microscale details of mountain winds. Bull Am Meteorol Soc 100:799–819

Finnigan J, Ayotte K, Harman I, Katul G, Oldroyd H, Patton E, Poggi D, Ross A, Taylor P (2020) Boundary-layer flow over complex topography. Boundary-Layer Meteorol 177:247–313

Freedman J, Fitzjarrald D (2017) Mechanisms responsible for the observed thermodynamic structure of a convective boundary layer over the Hudson Valley of New York State. Boundary-Layer Meteorol 164:89–106

Grachev A, Leo LS, Sabatino SD, Fernando HJS, Pardyjak ER, Fairall CW (2016) Structure of turbulence in katabatic flows below and above the wind-speed maximum. Boundary-Layer Meteorol 159:469–494

Grachev AA, Andreas E, Fairall C, Guest P, Persson P (2013) The critical Richardson number and limits of applicability of local similarity theory in the stable boundary layer. Boundary-Layer Meteorol 147:51–82

Grisogono B, Axelsen SL (2012) A note on the pure katabatic wind maximum over gentle slopes. Boundary-Layer Meteorol 145:527–538

Grisogono B, Rajak Z (2009) Assessment of Monin–Obukhov scaling over small slopes. Geofizika 26:101–108

Grisogono B, Kraljević L, Jeričević J (2007) The low-level katabatic jet height versus Monin–Obukhov height. Q J R Meteorol Soc 133:2133–2136

Grisogono B, Sun J, Belušić D (2020) A note on MOST and HOST for turbulence parameterization. Q J R Meteorol Soc 146:1991–1997

Guerra VS, Acevedo OC, Medeiros LE, Oliveira PES, Santos DM (2018) Small-scale horizontal variability of mean and turbulent quantities in the nocturnal boundary layer. Boundary-Layer Meteorol 169:395–411

Kang Y, Belušić D, Smith-Miles K (2015) Classes of structures in the stable atmospheric boundary layer. Q J R Meteorol Soc 141:2057–2069

Katul GG (2019) The anatomy of large-scale motion in atmospheric boundary layers. J Fluid Mech 858:1–4. https://doi.org/10.1017/jfm.2018.731

Kustas W, Li F, Jackson J, Preuger J, MacPherson J, Wolde M (2004) Effects of remote sensing pixel resolution on modeled energy flux variability of croplands in Iowa. Remote Sens Environ 92:535–547

Lang F, Belušić D, Siems S (2018) Observations of wind direction variability in the nocturnal boundary layer. Boundary-Layer Meteorol 166:51–68

Lapworth A, Osborne SR (2020) The nocturnal wind speed and sensible heat flux over flat terrain. Boundary-Layer Meteorol 176:401–413

Lehner M, Rotach M (2018) Current challenges in understanding and predicting transport and exchange in the atmosphere over mountainous terrain. Atmosphere https://doi.org/10.3390/atmos9070276

Leo L, Thompson M, Sabatino SD, Fernando HJS (2016) Stratified flow past a hill: dividing streamline concept revisited. Boundary-Layer Meteorol 159:611–634

Levy G, Vickers D (1999) Surface fluxes from satellite winds: modeling air-sea flux enhancement from spatial and temporal observations. J Geophys Res 104:20,639–20,650

Louis JF (1979) A parametric model of vertical eddy fluxes in the atmosphere. Boundary-Layer Meteorol 17:187–202

Mahrt L (2007) Weak-wind mesoscale meandering in the nocturnal boundary layer. Environ Fluid Mech 7:331–347

Mahrt L (2008) Bulk formulation of the surface fluxes extended to weak-wind stable conditions. Q J R Meteorol Soc 134:1–10

Mahrt L (2017) Lee mixing and nocturnal structure over gentle terrain. J Atmos Sci 74:1989–1999

Mahrt L (2020) Time-space variations of temperature in the nocturnal boundary layer. Q J R Meteorol Soc 146:2756–2767. https://doi.org/10.1002/qj.3815

Mahrt L, Sun J, Oncley SP, Horst TW (2014) Transient cold air drainage down a shallow valley. J Atmos Sci 71:2534–2544

Medeiros DG, Fitzjarrald D (2015) Stable boundary layer in complex terrain. Part II: geometrical and sheltering effects on mixing. J Appl Meteorol Climatol 54:170–188

Menke R, Vasiljević N, Mann J, Lundquist JK (2019) Characterization of flow recirculation zones at the Perdigão site using multi-lidar measurements. Atmos Chem Phys 29:851–875

Mortarini L, Stefanello M, Degrazia G, Roberti D, Castelli ST, Anfossi D (2016) Characterization of wind meandering in low-wind-speed conditions. Boundary-Layer Meteorol 161:165–182

Mortarini L, Cava D, Giostra U, Acevedo O, Nogueira Martins LG, Soares de Oliveira PE, Anfossi D (2018) Observations of submeso motions and intermittent turbulent mixing across a low level jet with a 132-m tower. Q J R Meteorol Soc 144:172–183

Nadeau DF, Pardyjak ER, Higgins CW, Huvald H, Parlange MB (2013) Flow during the evening transition over steep alpine slopes. Q J R Meteorol Soc 139:607–624

Oldroyd H, Katul G, Pardyjak E, Parlange W (2014) Momentum balance of katabatic flow on steep slopes covered with short vegetation. Geophys Res Lett 41:4761–4768

Oldroyd HJ, Pardyjak ER, Higgins C, Parlange MB (2016a) Buoyant turbulent kinetic energy production in steep-slope katabatic flow. Boundary-Layer Meteorol 159:539–565

Oldroyd HJ, Pardyjak ER, Huwald H, Parlange MB (2016b) Adapting tilt corrections and the governing flow equations for steep, fully three-dimensional, mountainous terrain. Boundary-Layer Meteorol 161:405–416

Pfister L, Sigmund A, Olesch J, Thomas CK (2017) Nocturnal near-surface temperature but not flow dynamics, can be predicted by microtopography in a mid-range mountain valley. Boundary-Layer Meteorol 165:333–348

Pfister L, Sayde C, Selker J, Mahrt L, Thomas CK (2019) Classifying the nocturnal boundary layer into temperature and flow regimes. Q J R Meteorol Soc 145:1515–1534

Poulos G, Blumen W, Fritts D, Lundquist J, Sun J, Burns S, Nappo C, Banta R, Newsome R, Cuxart J, Terradellas E, Balsley B, Jensen M (2001) A comprehensive investigation of the stable nocturnal boundary layer. Bull Am Meteorol Soc 83:555–581

Rotach MW, Zardi D (2007) On the boundary-layer structure over highly complex terrain: Key findings from MAP. Q J R Meteorol Soc 133:937–948

Rotach MW, Stiperski I, Furher O, Goger B, Gohm A, Obleitner F, Rau G, Sfyri E, Vergeiner J (2017) Investigating exchange processes over complex topography: the Innsbruck Box (I-Box). Bull Am Meteorol Soc 98:787–805

Salesky ST, Anderson W (2018) Buoyancy effects on large-scale motions in convective atmospheric boundary layers; implications for modulation of near-wall processes. J Fluid Mech 856:135–168

Salesky ST, Anderson W (2020) Coherent structures modulate atmospheric surface layer flux-gradient relationships. Phys Rev Lett https://doi.org/10.1103/PhysRevLett.125.124501

Shapiro A, Fedorovich E, Rahimi S (2016) A unified theory for the Great Plains nocturnal low-level jet. J Atmos Sci 73:3037–3057

Sheridan P, Vosper S, Smith S (2018) A case-study of cold-air pool evolution in hilly terrain using field measurements from COLPEX. J Appl Meteorol Climatol 57:1907–1929

Staebler R, Fitzjarrald D (2004) Observing subcanopy CO2 advection. Agric For Meteorol 122:139–156

Stefanello M, Cava D, Giostra U, Acevedo O, Degrazia G, Anfossi D, Mortarini L (2020) Influence of submeso motions on scalar oscillations and surface energy balance. Q J R Meteorol Soc 146:889–903

Stiperski I, Rotach MW (2016) On the measurement of turbulence over complex mountainous terrain. Boundary-Layer Meteorol 159

Stoll R, Porté-Agel F (2009) Surface heterogeneity effects on regional-scale fluxes in stable boundary layers: surface temperature transitions. J Atmos Sci 15:1392–1404

Sun J, Mahrt L, Nappo C, Lenschow D (2015a) Wind and temperature oscillations generated by wave-turbulence interactions in the stably stratified boundary layer. J Atmos Sci 71:1484–1503

Sun J, Nappo CJ, Mahrt L, Belušić D, Grisogono B, Stauffer DR, Pulido M, Staquet C, Jiang Q, Pouquet A, Yagüe C, Galperin B, Smith RB, Finnigan JJ, Mayor SD, Svensson G, Grachev AA, Neff WD (2015b) Review of wave-turbulence interactions in the stable atmospheric boundary layer. Rev Geophys 53:965–993

Sun J, Tackle ES, Acevedo O (2020) Understanding physical processes represented by the Monin–Obukhov bulk formula for moment transfer. Boundary-Layer Meteorol 177:69–95

Urbancic GH, Suomi I, Vihma T (2020) A general theory for the characterization of submeso-scale motions and turbulence in the atmospheric surface layer. Q J R Meteorol Soc 147:660–678

Van de Wiel BJH, Moene A, Hartogenesis G, Bruin HD, Holtslag AAM (2003) Intermittent turbulence in the stable boundary layer over land. Part III: a classification for observations during CASES-99. J Atmos Sci 60:2509–2522

Van den Bossche M, De Wekker SFJ (2018) Representativeness of wind measurements in moderately complex terrain. Theor Appl Climatol 135:491–504

Vercauteren N, Mahrt L, Klein R (2016) Investigation of interactions between scales of motion in the stable boundary layer. Q J R Meteorol Soc 142:2424–2433

Vercauteren N, Boyko V, Kaiser A, Belušić D (2019) Statistical investigations of flow structures in different regimes of the stable boundary layer. Boundary-Layer Meteorol 173:143–164

Viana S, Terradellas S, Yagüe C (2010) Analysis of gravity waves generated at the top of a drainage flow. J Atmos Sci 67:3949–3966

Vickers D, Esbensen S (1998) Subgrid surface fluxes in fair weather conditions during TOGA COARE: observational estimates and parameterization. Mon Weather Rev 126:620–633

Williams A (2001) A physically based parameterization for surface flux enhancement by gustiness in dry and precipitating convection. Q J R Meteorol Soc 127:469–491

Williams A, Chambers S, Griffiths S (2013) Bulk mixing and decoupling of the stable nocturnal boundary layer characterized using a ubiquitous natural tracer. Boundary-Layer Meteorol 149:381–402

Žagar N, Žagar M, Cedilnik J, Gregorič G, Rakovec J (2006) Validation of mesoscale low-level winds obtained by dynamical downscaling of ERA40 over complex terrain. Tellus 58:445–455

Zhou B, Chow FK (2014) Nested large-eddy simulations of the intermittently turbulent stable atmospheric boundary layer over real terrain. J Atmos Sci 71:1021–1039